Comprehensive analysis of electrically-pumped GaSb-based VCSELs

S. Arafin,[1,*] **A. Bachmann,**[1] **K. Vizbaras,**[1] **A. Hangauer,**[1]
J. Gustavsson,[2] **J. Bengtsson,**[2] **A. Larsson,**[2] **and M.-C. Amann**[1]

[1]*Walter Schottky Institut, Technische Universität München, Am Coulombwall 3, 85748 Garching, Germany*
[2]*Department of Microtechnology and Nanoscience, Chalmers University of Technology, SE-412 96 Göteborg, Sweden*

[*]arafin@wsi.tum.de

Abstract: This paper discusses several performance-related aspects of electrically-pumped GaSb-based buried tunnel junction VCSELs with an emission wavelength of 2.6 µm based on theoretical and experimental results. These results allow a deeper insight into the internal device physics, such as radial diffusion of carriers, maximum continuous-wave operating temperature, diffraction loss, internal temperature, gain and loss parameters, internal quantum efficiency of the active region etc. These parameters can be taken into account while designing mid-infrared lasers which leads to an improved device performance. A simple thermal model of the devices based on the two-dimensional (2-D) finite element method using the material data from the literature is also presented. In addition, an application-based result utilizing these lasers for the measurement of absolute water vapor concentration by wavelength modulation spectroscopy (WMS) method are also described, hinting that devices are well-suited for the targeted sensing applications.

© 2011 Optical Society of America

OCIS codes: (140.7260) Vertical cavity surface emitting lasers; (140.5960) Semiconductor lasers.

References and links

1. L. S. Rothman, D. Jacquemart, A. Barbe, D. C. Benner, M. Birk, L. R. Brown, M. R. Carleer, C. Chackerian, Jr., K. Chance, L. H. Coudert, V. Dana, V. M. Devi, J.-M. Flaud, R. R. Gamache, A. Goldman, J.-M. Hartmann, K. W. Jucks, A. G. Maki, J.-Y. Mandin, S. T. Massie, J. Orphal, A. Perrin, C. P. Rinsland, M. A. H. Smith, J. Tennyson, R. N. Tolchenov, R. A. Toth, J. Vander Auwera, P. Varanasi, and G. Wagner, "The HITRAN 2004 molecular spectroscopic database," J. Quant. Spectrosc. Radiat. Transfer **96,** 139–204 (2005).
2. W. W. Bewley, C. L. Felix, I. Vurgaftman, E. H. Aifer, J. R. Meyer, L. Goldberg, J. R. Lindle, D. H. Chow, and E. Selvig, "Continuous-wave mid-infrared VCSELs," IEEE Photon. Technol. Lett. **10,** 660–662 (1998).
3. N. Schulz, J.-M. Hopkins, M. Rattunde, D. Burns, and J. Wagner, "High-brightness long-wavelength semiconductor disk lasers," Laser & Photon. Rev. **2,** 160–181 (2008).
4. F. Genty, A. Garnache, and L. Cerutti, "VCSELs emitting in the 2-3 µm wavelength range," in *Mid-infrared Semiconductor Optoelectronics*, A. Krier, ed. Springer Series in Optical Sciences (Springer, 2006), Vol. 118, pp. 159–188.
5. A. Ducanchez, L. Cerutti, P. Grech, F. Genty, and E. Tournie, "Mid-infrared GaSb-based EP-VCSEL emitting at 2.63 µm," Electron. Lett. **45,** 265–267 (2009).
6. R. S. Inman, and J. J. F. McAndrew, "Application of tunable diode laser absorption spectroscopy to trace moisture measurements in gases," Anal. Chem. **66,** 2471–2479 (1994).
7. A. Bachmann, K. Kashani-Shirazi, and M.-C. Amann, "GaSb-based electrically pumped VCSEL with buried tunnel junction operating continuous wave up to 50ºC," in *Proceedings of IEEE Conference on Semiconductor Laser* (Institute of Electrical and Electronic Engineers, Italy, 2008), paper TuA1, pp. 39–40.

8. S. Arafin, A. Bachmann, K. Kashani-Shirazi, and M.-C. Amann, "Electrically-pumped continuous-wave vertical-cavity surface-emitting lasers at 2.6 μm," Appl. Phys. Lett. **95,** 131120 (2009).

9. J. Chen, A. Hangauer, A. Bachmann, T. Lim, K. Kashani-Shirazi, R. Strzoda, and M.-C. Amann, "CO and CH_4 sensing with single mode 2.3 μm GaSb-based VCSEL," in *Conference on Lasers and Electro-Optics* (Optical Society of America, Baltimore, MD, 2009), paper CThI.

10. A. Hangauer, J. Chen, R. Strzoda, M. Ortsiefer, and M.-C. Amann, "Wavelength modulation spectroscopy with a widely tunable InP-based 2.3 μm vertical-cavity surface-emitting laser," Opt. Lett. **33,** 1566–1568 (2008).

11. A. Hangauer, J. Chen, R. Strzoda, and M.-C. Amann, "The frequency modulation response of vertical-cavity surface-emitting lasers: experiment and theory," IEEE J. Sel. Top. Quantum Electron. **17,** 1–10 (2011).

12. A. Bachmann, S. Arafin, and K. Kashani-Shirazi, "Single-mode electrically pumped GaSb-based VCSELs emitting continuous-wave at 2.4 and 2.6 μm," N. J. Phys. **11,** 125014 (2009).

13. A. Bachmann, K. Kashani-Shirazi, S. Arafin, and M.-C. Amann, "GaSb-based VCSEL with buried tunnel junction for emission around 2.3 μm," IEEE J. Sel. Top. Quantum Electron. **15,** 933–940 (2009).

14. http://www.comsol.com/

15. S. Adachi, "Lattice thermal conductivity of group-IV and III-V semiconductor alloys," J. Appl. Phys. **102,** 063502 (2007).

16. T. Borca-Tasciuca, D. W. Song, J. R. Meyer, I. Vurgaftman, M.-J. Yang, B. Z. Noshob, and L. J. Whitman, and G. Chen, "Thermal conductivity of $AlAs_{0.07}Sb_{0.93}$ and $Al_{0.9}Ga_{0.1}As_{0.07}Sb_{0.93}$ alloys and $(AlAs)_1/(AlSb)_{11}$ digital-alloy superlattices," J. Appl. Phys. **92,** 4994–4998 (2002).

17. M. Osinski, and W. Nakwaski, "Effective thermal conductivity analysis of 1.55 μm InGaAsP/InP vertical-cavity top-surface-emitting microlasers," Electron. Lett. **29,** 1015–1016 (1993).

18. M. Ortsiefer, "Langwellige Vertikalresonator-Laserdioden im Materialsystem InGaAlAs/InP," PhD thesis (Technische Universität München, 2000).

19. K. L. Lear, R. P. Schneider, Jr., K. D. Choquette, and S. P. Kilcoyne, "Index guiding dependent effects in implant and oxide confined vertical-cavity lasers," IEEE Photon. Technol. Lett. **8,** 740–742 (1996).

20. S. Arafin, A. Bachmann, and M.-C. Amann, "Transverse-mode characteristics of GaSb-based VCSELs with buried-tunnel junctions," IEEE J. Sel. Top. Quantum Electron. **9,** 1–8 (2011).

21. A. N. Al-Omari, and K. L. Lear, "VCSELs with a self-aligned contact and copper-plated heatsink," IEEE Photon. Technol. Lett. **17,** 1767–17697 (2005).

22. R. Michalzik, M. Grabherr, R. Jaeger, M. Miller, and K. J. Ebeling, "Progress in high-power VCSELs and arrays," Proc. SPIE **3419,** 187–195 (1998).

23. D. I. Babic, Y. Chung, N. Dagli, and J. E. Bowers, "Modal reflection of quarter-wave mirrors in vertical-cavity lasers," IEEE J. Quantum Electron. **29,** 1950–1962 (1993).

24. J. W. Goodman, *Introduction to Fourier Optics* (McGraw-Hill, 1996).

25. A. Perona, A. Garnache, L. Cerutti, A. Ducanchez, S. Mihindou, P. Grech, G. Boissier and F. Genty, "AlAsSb/GaSb doped distributed Bragg reflectors for electrically pumped VCSELs emitting around 2.3 μm," Semicond. Sci. Technol. **22,** 1140–1144 (2007).

26. A. Hangauer, J. Chen, and M.-C. Amann, "Vertical-cavity surface-emitting laser light-current characteristic at constant internal temperature," IEEE Photon. Technol. Lett. available online, DOI: 10.1109/LPT.2011.2160389 (2011).

27. G. M. Yang, M. H. MacDougal, V. Pudikov, and P. D. Dapkus, "Influence of mirror reflectivity on laser performance of very-low-threshold vertical-cavity surface-emitting lasers," IEEE Photon. Technol. Lett. **7,** 1228–1230 (1995).

28. C. Bückers, A. Thränhardt, S. W. Koch, M. Rattunde, N. Schulz, J. Wagner, J. Hader, and J. V. Moloney, "Microscopic calculation and measurement of the laser gain in a (GaIn)Sb quantum well structure," Appl. Phys. Lett. **92,** 071107 (2008).

29. E. R. T. Kerstel, R. Q. Iannone, M. Chenevier, S. Kassi, H.-J. Jost, and D. Romanini, "A water isotope (^{2}H, ^{17}O, and ^{18}O) spectrometer based on optical feedback cavity-enhanced absorption for in situ airborne applications," Appl. Phys. B: Lasers Opt. **85,** 397–406 (2006).

30. J. T. C. Liu, J. B. Jeffries, and R. K. Hanson, "Wavelength modulation absorption spectroscopy with 2f detection using multiplexed diode lasers for rapid temperature measurements in gaseous flows," Appl. Phys. B: Lasers Opt. **78,** 503–511 (2004).

31. R. Arndt, "Analytical line shapes for Lorentzian signals broadened by modulation," J. Appl. Phys. **36,** 2522–2524 (1965).

1. Introduction

Over the last couple of years, significant progress has been made towards the development of mid-infrared (MIR) GaSb-based semiconductor lasers in the wavelength range 2-3.5 μm. In fact, there are strong absorption lines of numerous trace gases like CO, H_2S, H_2O, HF, CH_4, CO_2 etc. in this spectral regime [1]. In the family of semiconductor lasers, vertical-cavity

surface-emitting lasers (VCSELs) are the most promising light sources which are being currently used in lots of significant applications. Several groups worldwide are currently involved in realizing GaSb-based surface-emitting lasers. Bewley et al. [2], Rattunde et al. [3] and Genty et al. [4] have already reported optically-pumped Sb-based VCSELs in the range of 2-3 µm for sensing applications. However, optical pumping significantly increases the complexity and the cost of the overall system due to the use of an additional pump laser which itself requires much more electrical power. The realization of a compact design seems to be difficult in this way. Recently, monolithic electrically-pumped (EP) GaSb-based VCSELs in pulse operation emitting at 2.63 µm have been achieved which is the longest wavelength ever reported for any EP-VCSELs [5]. But such devices without any current aperture exhibit multimode operation. Thus devices lose its usability in gas sensing applications since lasers with single-mode emission are required in gas sensing applications by tunable diode laser absorption spectroscopy (TD-LAS) [6]. EP and CW-operating GaSb-based single-mode VCSELs emitting at 2.3-2.6 µm [7,8] have also been demonstrated recently and proven to be application-suited [9]. Note that wavelengths higher than 2.3 µm are only accessible with the GaSb material system, because this seems to be the wavelength limit where TDLS suitable VCSELs on the InP material system are available [10]. Furthermore, the maximum tuning speed for the 2.3 µm GaSb based is significantly higher and the FM response is more flat than for the 2.3 µm InP based VCSEL which enhances the applicability of GaSb-based VCSELs [11].

Despite the promising performance of GaSb-based VCSELs, their development towards large scale applications has been greatly hindered by the immature and complicated growth technique of this material system and insufficient knowledge on material data for the device design. Finding the optimum design by device modeling numerically or analytically sometimes does not give the real device picture due to a lot of unknown issues. This paper provides a clear insight into the physics of already realized VCSELs at 2.6 µm which can be utilized as guidelines for realistic modeling of future devices. As a result, the device performance is likely to be improved in future.

A thorough experimental and theoretical analysis of index-guided GaSb-VCSELs is addressed in this study. This index guiding in the device is obtained by an effective refractive index step due to the presence of a buried tunnel junction (BTJ) concept. This paper is organized as follows. Section 2 presents the device schematics and a detailed discussion of the thermal properties of such devices. We then demonstrate the various experimental results on device size dependent threshold current yielding carrier diffusion length, diffraction loss, internal temperature and extraction of laser parameters and then determine the optimum number of quantum wells (QWs). The applicability of 2.6 µm VCSELs is also demonstrated for the first time by wavelength modulation spectroscopy (WMS) of H_2O. Finally, Section IV concludes the paper.

2. Device Design

A schematic illustration of the MBE-grown GaSb-based BTJ VCSELs is shown in Fig.1, where D_{BTJ} denotes the aperture diameter of the device. The electric current injected around the dielectric mirror is effectively confined by the structured tunnel junction. Details of the electrical and optical design and all fabrication steps required to realize the device are mentioned in [12, 13]. As a part of the device design, this section will focus only on the thermal design of such devices.

2.1. Thermal Design

Thermal modeling is one of the key design issues for devices utilizing the low bandgap material system, GaSb. Generally the device performance, i.e., optical output power and threshold
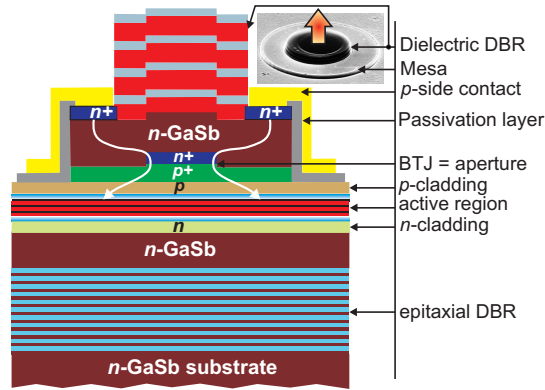
Fig. 1. Schematic cross-sectional view of the GaSb-based VCSEL structure with BTJ. The current path is shown. The upper right corner is the SEM photograph of the top-emitting device after fabrication.

current is limited by thermal effects. To gain a deep insight into GaSb-based BTJ VCSELs, at first the theoretical and systematic thermal analysis using a heat dissipation model will be presented here. The device thermal parameters, such as internal temperature distribution, heat flux, and thermal resistance can be extracted out of the model based on the two-dimensional (2-D) rotationally symmetric, steady-state heat transfer model. The analysis was done by using COMSOL Multiphysics finite element analysis simulation software [14]. The thermal conductivities of the individual layers in GaSb-based BTJ VCSELs are taken from the literature [15, 16] and summarized in Table 1 along with brief details and the thickness of that corresponding layer. In this analysis, the effective thermal conductivities with anisotropy were used for thin multilayers, e.g. active region. The effective thermal conductivities in lateral and vertical directions are given by [17]

$$k_l = \frac{d_1 k_1 + d_2 k_2}{d_1 + d_2}, \qquad k_v = \frac{d_1 + d_2}{d_1/k_1 + d_2/k_2} \tag{1}$$

where k_1/k_2 and d_1/d_2 are the thermal conductivity and thickness for layer 1/layer 2, respectively. For the active region and bottom epitaxial Bragg mirror, the effective thermal conductivity value is used defined by Eq. (1). Here, reduced values are expected that are caused by phonon mean free path restrictions in thin layers.

As shown in Fig. 2 b), a large amount of heat from the active region flow laterally and vertically downward toward the GaSb substrate through bottom epitaxial DBR and also laterally toward the top p-side Au-contact. This has been indicated by long white arrows, showing the heat rapidly spreads out over a wide area in the radial direction. The heat source is sandwiched by top and bottom GaSb heat spreading layer which also contributes to dissipate the heat. The active region diameter, $D_{BTJ} + 2r_{diff} = 5.5 \, \mu m + 3.4 \, \mu m = 8.9 \, \mu m$ has been considered in this simulation by taking the effective pumped area of the device into account, where r_{diff} is the carrier diffusion length discussed in Sect. 3.1. Since the wallplug efficiency is nearly zero at threshold, all input electrical power is assumed to be dissipated in the form of heat. Thus, the volumetric heat source density, Q can be determined from experimental threshold parameters by

$$Q = \frac{I_{th} \cdot V_{ac}}{V} = \frac{I_{th} \cdot V_{ac}}{\frac{\pi}{4} \cdot (D_{BTJ} + 2r_{diff})^2 \cdot h} \tag{2}$$

where, V_{ac} and I_{th} are the voltage drop across the active region and threshold current, respectively, V and h are the volume and thickness of the active region, respectively. The voltage
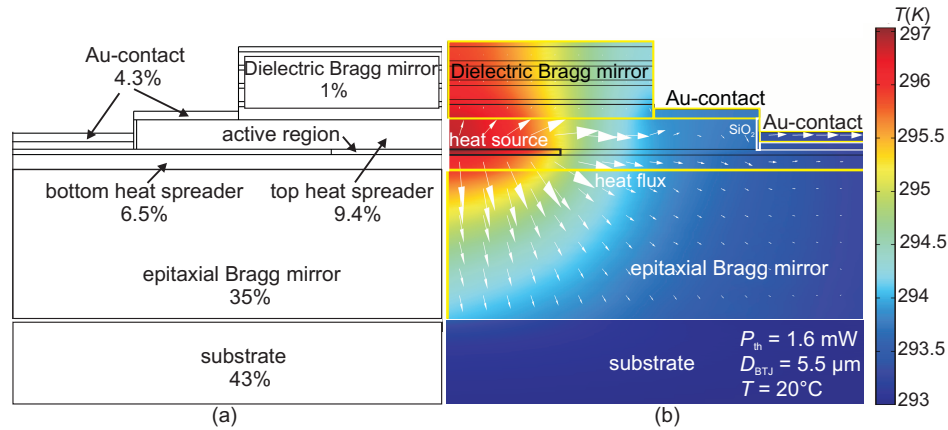
Fig. 2. a) Two-dimensional (2-D) GaSb-based top emitting VCSEL structure employing a rotational structural symmetry along the z-axis used in the simulation. The contribution of different layers of the device in dissipating the heat is shown in percentage as well. b) 2-D steady state heat flux and temperature distribution. The black rectangle represents the QW region which has been assumed to be the main heat source in this simulation. The bottom epitaxial Bragg mirror on top of 500 μm thick GaSb substrate and top dielectric Bragg mirror have been marked with yellow border lines. White arrows represent the magnitude and the direction of the heat flow.

Table 1. Thermal Conductivity for Different Layers in GaSb-Based BTJ VCSELs

Description	Material	Thickness (nm)	k (W/m-k)
Top p-side contact	Au	300	317
Passivation layer	SiO_2	250	1.4
Top dielectric DBR	a-Si/SiO_2	188/455	1.8/1.4
Top current spreading layer	GaSb	1120	32 [15]
Bottom current spreading layer	GaSb	520	32 [15]
Top n-side contact	Au	300	315
Bottom epitaxial DBR	$AlAs_{0.08}Sb$/GaSb	200/170 (24 pairs)	19.8 [16]/32 [15] k_l= 20, k_v = 14.4
Active region (QW/Barrier)	$In_{0.43}GaAs_{0.14}Sb$/GaSb	10/8	4/32 [15], k_l= 16, k_v = 5

drop across the active region is obtained by subtracting ohmic drop arising from the laser series resistance from the measured threshold voltage, V_{th}

$$V_{ac} = V_{th} - I_{th} \cdot R_s \qquad (3)$$

where, R_s is the series resistance. The measured threshold current, threshold voltage and series resistance of the device with D_{BTJ} = 5.5 μm are 3.2 mA, 0.62 V, and 33 Ω, respectively. So, V_{ac} can be calculated to ≈ 0.51 V. Thus the total dissipated heat power in the active region is 1.6 mW. The rest of the power ≈ 0.4 mW is assumed to be dissipated as joule heating in the other layers whose effect to rise in active region temperature is almost negligible. Using these values in the simulation, the maximum heating of ΔT = 4 K in the active region with respect to the heatsink temperature is obtained which corresponds to a thermal resistance of ≈ 1995 K/W,

showing a good agreement with the experimental value mentioned in Sect. 3.2.

As displayed in Fig. 2 a) most of the heat (78%) generated in the active region flow downward mainly to the copper heatsink by conduction through the GaSb substrate (43%) and epitaxial bottom DBR (35%). The rest of the heat is mainly transferred to the air by radiation and natural convection through the top p-side Au contact. The top dielectric DBR hardly conducts any heat due to the low thermal conductivities of dielectric materials. Since the presented devices with upside up concept already show good thermal properties, the upside-down concept would even improve the thermal management in such devices.

3. Experimental Details

3.1. Carrier Diffusion Length

The threshold current density in any aperture VCSELs is mainly scaled by the current spreading and the lateral carrier diffusion in the active region. Current spreading takes place in the region between the current aperture and the active region. In our BTJ VCSELs, the vertical distance between the BTJ aperture and the active region is roughly 100 nm, so the influence of the current-spreading phenomenon on the threshold current is negligible. Also, if one assumes the thin region below the aperture is low-doped, then the assumption is valid. Hence the threshold current density of the devices under study is mainly governed by the radial carrier diffusion in the active region. That means that the carrier diffusion length needs to be experimentally measured in order to determine the threshold current density accurately. The threshold current, I_{th} in VCSELs can be expressed with the threshold current density, J_{th} by the following equation:

$$I_{th} = \frac{\pi}{4}(D_{BTJ} + 2r_{diff})^2 J_{th} \propto (D_{BTJ} + 2r_{diff})^2 \tag{4}$$

where, r_{diff} is the lateral carrier diffusion length. It is evident that I_{th} is proportional to the square of the BTJ aperture diameter plus an extension caused by the carrier diffusion on both sides of the BTJ. Clearly, this is the area of the active region which is being effective pumped during device operation. Figure 3 shows the measured CW threshold current against BTJ aperture diameter for 2.3 μm and 2.6 μm VCSELs at a constant device internal temperature. In fact, devices with different aperture diameters have different internal heating at constant heatsink temperature. So, it is important to measure the threshold current of VCSELs at constant internal temperature which is simply the sum of the heatsink temperature and the temperature rise, ΔT in the active region of the device at threshold. ΔT value can be obtained by measuring the thermal resistance, R_{th} and the applied threshold power, P_{th} for each device.

$$\Delta T = R_{th} \cdot \Delta P_{th} \tag{5}$$

Note that the proportionality behavior indicated in Eq. (4) is valid up to the device with a certain BTJ diameter since J_{th} starts to increase at small aperture diameters which can be attributed by the diffraction loss present in such devices. By plotting the square root of the threshold current against BTJ diameter, one can calculate the diffusion length from the intercept of the x-axis. A diffusion length of $r_{diff} \approx 1.7$ μm on each side of the BTJ is evaluated in Fig. 3 for both 2.3 μm and 2.6 μm VCSELs, being in good accordance with values determined for other BTJ-VCSELs [18]. Once the diffusion length is experimentally determined, the effective threshold current density can be calculated as shown in inset of Fig. 3. Interestingly, both 2.3 μm and 2.6 μm VCSELs show the minimum of the threshold current at the device size of approximately 4 μm diameter, hinting that these devices are strongly index guided. If the device would be weakly index guided, e.g. implanted VCSELs, the minimum of the threshold current would shift to device with larger aperture diameter where the diffraction loss would start to
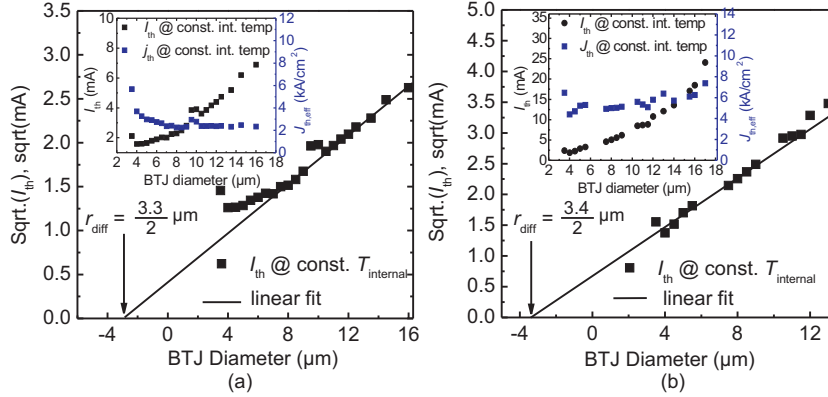
Fig. 3. Square root of the measured CW threshold current at constant internal temperature against BTJ diameter of VCSELs emitting at a) 2.35 μm and b) 2.6 μm. Extracting the carrier diffusion length from these figures and taking that into account, the threshold current densities in such devices have been calculated shown as displayed in inset. The increase of the threshold current in devices with small aperture diameters is due to the high diffraction losses.

dominate earlier with decreasing device size [19]. As a matter of fact, the strong index guiding in GaSb-based BTJ VCSELs is achieved by an high effective refractive index step due to the presence of a laterally structured BTJ in the cavity [20].

3.2. Maximum CW operating temperature

Figure 4 a) shows the maximum CW operating temperature, T_{max} against BTJ diameter ranging from 3.5 μm to 20 μm. It is seen that T_{max} decreases with the increase of the BTJ diameter except $D_{BTJ} \leq 4$ μm. In other words, the smaller devices are suitable for higher temperature operation in cw mode. In order to identify the reason of this behavior, we measured the thermal resistance of each device as displayed in Fig. 4 b). The decrease of the thermal resistance with device diameter does not follow $1/D_{BTJ}$ behavior as expected for top emitting VCSELs. Therefore, the heat removal in such BTJ VCSELs is not one-dimensional, three-dimensional instead. The thermal resistance can be measured or extracted from the shift of emission wavelength to longer wavelength with increasing temperature and with increasing current which can be mathematically written as follows:

$$R_{th} = \frac{\frac{\Delta\lambda}{\Delta P_{el}}\big|_{T=const.}}{\frac{\Delta\lambda}{\Delta T}\big|_{P_{el}=const.}} \qquad (6)$$

Here, $\frac{\Delta\lambda}{\Delta P_{el}}\big|_{T=const.}$ is the power tuning coefficient at a constant heatsink temperature and $\frac{\Delta\lambda}{\Delta T}\big|_{P_{el}=const.}$ is the thermal tuning coefficient at a constant applied electrical power. At this point, Table 2 can be introduced in order to demonstrate a comparison of thermal resistance among VCSELs with active region diameter between 5 μm and 13 μm based on different material system. Thus one can have a better feeling about the thermal performance in devices under study. In particular, the thermal resistance value of the InP-based BTJ VCSEL mentioned in Table 2 is for the structure mounted epi-side-down onto an integrated Au-heatsink. Since the presented top-emitting GaSb-based devices without any integrated heatsink show a reasonably good thermal properties, this proves a good thermal design.

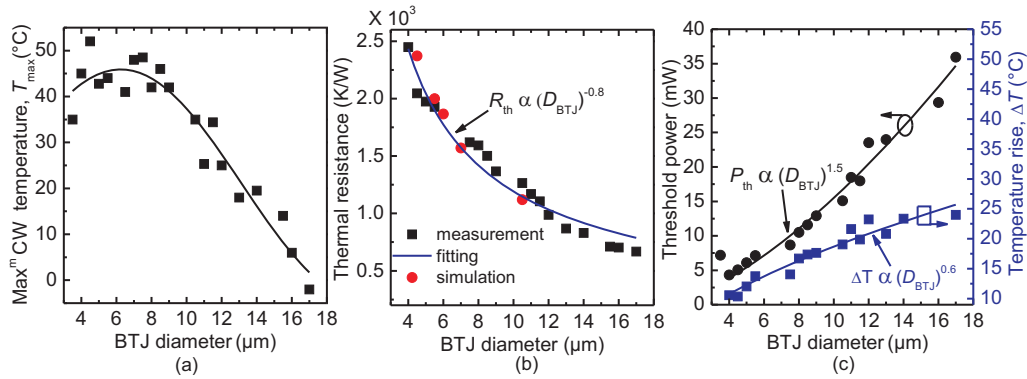As a part of the investigation to identify the reason of having a lower T_{max} at device with

Fig. 4. The dependence of a) maximum CW lasing temperature ($T_{\max}$) and b) thermal resistance at 20°C as a function of BTJ diameter of 2.6 μm VCSELs. The measured thermal resistance points are obtained by Eq. (6), whereas, the simulated (red-marked) points are by the finite element method (FEM) simulation, showing a good agreement. The curve fitting was done to the measured data. c) The consumed threshold power at a constant internal temperature and the temperature rise of the active region with respect to the heatsink temperature against BTJ diameter of 2.6 μm VCSELs. The continuously increasing temperature rise of the devices with BTJ diameters indicates that the device performance can be further improved by a better thermal design.

Table 2. Thermal Conductivity for VCSELs with Active Diameter, $5\,\mu m \leq D_a \leq 13\,\mu m$ ($D_a \equiv D_{\mathrm{BTJ}}$) on Different Material System

	GaAs-based	InP-based	GaSb-based
Thermal resistance (K/W)	$1350 \leq R_{\mathrm{th}} \leq 3650$ [21]	$3500 \leq R_{\mathrm{th}} \leq 700$ [18]	$1980 \leq R_{\mathrm{th}} \leq 870$

a larger diameter, the electrical CW threshold power, P_{th} consumed by the device at constant internal temperature is measured for VCSELs of different size. It is found that P_{th} is increasing at a higher rate than the decreasing rate of thermal resistance with increasing device size as demonstrated in Fig. 4 c). This is why the maximum CW lasing temperature decreases with the increase of the aperture diameter. For the device with very small aperture diameter, the threshold current increases again due to the high diffraction losses (see next section) which leads to an increasing CW threshold power, resulting a lower CW operating temperature. The lower decreasing rate of thermal resistance and the higher increasing rate of consumed threshold power with increasing device aperture diameter give a dependence of temperature rise in the active region on the device size. As illustrated in Fig. 4 c), the temperature rise is scaled by the relation $\Delta T \propto D_{\mathrm{BTJ}}^{0.6}$. However, the temperature rise in the devices would be independent of device size if R_{th} and P_{th} would obey the scaling law $\propto D_a^{-1}$ and $\propto D_a$, respectively, where D_a is the active diameter, as expected for top emitting GaAs-based VCSELs [22].

3.3. Diffraction loss

In most VCSELs, the cavity propagation loss is mainly due to outcoupling through the Bragg mirrors and optical absorption in the semiconductor material. In addition to these two loss types, there is the diffraction loss, which is the excess loss caused by the fact that light does not propagate only in the longitudinal direction. Like all beams of light, the cavity field has a tendency to spread, i.e. to propagate also in the radial direction, which causes a radial leakage

of radiation along the entire length of the cavity. For most VCSELs, this leakage - the diffraction loss - is small, since the typical VCSEL cavity is short in the longitudinal direction and relatively wide in the lateral direction. So this type of loss can be neglected in most VCSELs. However, because of the BTJ and the resulting change in the topology of all layers above it, the intracavity field in the GaSb-based BTJ VCSEL experiences a strongly varying refractive index also in the lateral direction. This lateral disturbance results in an enhanced spreading of the light, thus considerably increasing the diffraction loss.

A direct measurement of the diffraction loss is very difficult; on the other hand, since diffrac-

VCSEL @ 2.6 μm loss budget ($D_{BTJ} = 8$ μm)

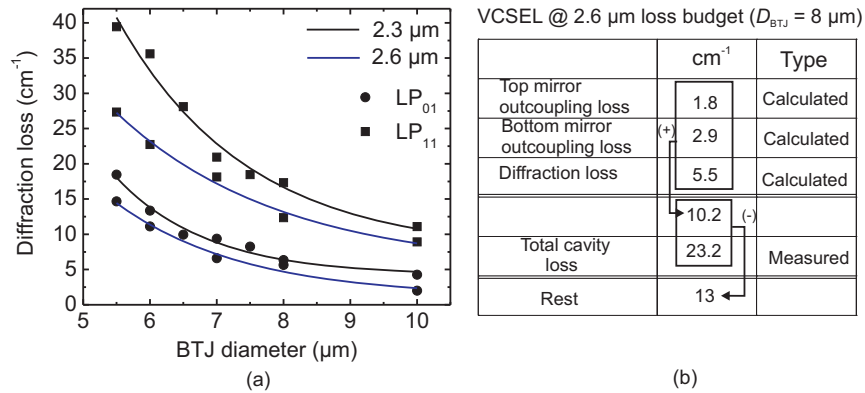|	cm^{-1}	Type
Top mirror outcoupling loss	1.8	Calculated
Bottom mirror outcoupling loss	(+) 2.9	Calculated
Diffraction loss	5.5	Calculated
	→ 10.2 (-)	
Total cavity loss	23.2	Measured
Rest	13 ←	

(a)   (b)

Fig. 5. a) Simulated diffraction loss as a function of the BTJ diameter. Two different cavities are analyzed, the 2.3 μm VCSEL and the 2.6 μm VCSEL, the latter with a smaller BTJ-induced step in the cavity structure, thereby reducing the diffraction loss. For each cavity the diffraction loss for the fundamental mode field (LP_{01}) and for the first higher order mode field (LP_{11}) is calculated. b) Calculation of loss budget for 2.6 μm VCSELs with $D_{BTJ} = 8$ μm.

tion is caused by the spatially varying real part of the refractive index, without being much influenced by, e.g., the QW gain or material absorption, it can be estimated with fair accuracy by numerical simulation, provided that the numerical model of the complicated VCSEL structure does not overwhelm the computer resources. Therefore we implemented a numerical method for calculating the intracavity field, and the radial field leakage, that is efficient in terms of computer memory. It is a hybrid method using a 3D transfer matrix method (TMM) [23] for the VCSEL structure beneath the BTJ, where there is no lateral variation in the refractive index, and a beam propagation method (BPM) [24] for the BTJ and the structure above it. As a result we obtained the diffraction loss as a function of the BTJ diameter as shown in Fig. 5 a). As expected the diffraction loss increases when the BTJ diameter is decreased, and for $D_{BTJ} \leq$ 8 μm the diffraction loss is of the same order of magnitude as the outcoupling loss through the mirrors; this can lead to an increased threshold current for VCSELs with a small BTJ.

Figure 5 a) also shows that the diffraction loss was somewhat lower for the 2.6 μm VCSEL. To understand this we can view the BTJ as an aperture for the intracavity field. It is a more complicated structure than a simple aperture, but the trends of the behavior with respect to the diffraction loss should be the same. Thus we would expect that going from 2.3 μm to 2.6 μm would result in an increased diffraction loss because the aperture becomes smaller measured in wavelength, leading to an increase in the off-axis diffraction. This was also confirmed in simulations, showing a 30% increase in the loss, in rough accordance with the theory for a simple aperture. On the other hand, the longer wavelength means that also the BTJ-induced step height is smaller measured in wavelength which should lower the diffraction loss. These two effects

would thus partly balance each other; simulations showed that the net result would still be an increase of the diffraction loss as we go to 2.6 μm . Therefore we modified the 2.6 μm VCSEL cavity by reducing also the physical BTJ-induced step height from 72 nm in the 2.3 μm VC-SELs to 55 nm. This strategy was successful, giving a small net reduction of the diffraction loss compared to the shorter-wavelength device, as indicated in Fig. 5 a). Finally, this figure shows that diffraction loss can be an important mode selecting mechanism. It strongly favors single mode operation in the fundamental LP_{01} mode thanks to the large loss difference to the first higher order mode.

Also the other loss mechanisms in VCSELs, such as outcoupling loss for both top and bottom mirrors obtained by the calculation is listed in Fig. 5 b). The total cavity loss has been measured to be as high as 23.2 cm^{-1}. The experimental procedure involved in obtaining the total loss value will be described in Sect. 3.5. So, the remaining loss of 13 cm^{-1} can be attributed to the free-carrier absorption (FCA) losses in the epitaxial mirror, QW active region and the 3λ thick GaSb cavity. Out of those remaining losses, the average FCA loss in the epitaxial mirror can be calculated by the following relation

$$\bar{\alpha}_m^{FCA} = \frac{n_L \alpha_H + n_H \alpha_L}{n_H + n_L} \tag{7}$$

where $\bar{\alpha}_m^{FCA}$ is the average absorption coefficient in the epitaxial mirror, n_L and n_H are the low and high refractive indices of the mirror material and the absorption coefficient in the high and low index material are denoted with α_H and α_L. For the emission wavelength of 2.6 μm, we have, $n_{AlAsSb} = 3.19$, $n_{GaSb} = 3.83$, $\alpha_{AlAsSb} = 13.2$ cm^{-1} and $\alpha_{GaSb} = 10.1$ cm^{-1} which yields $\bar{\alpha}_m^{FCA} = 11.7$ cm^{-1}, whereas the optical absorption losses in such DBRs were measured to be 5-10 cm^{-1} at 2.3 μm [25].

3.4.   Internal Temperature

Neither the direct measurement nor the analytical analysis or modeling can accurately tell the internal temperature of VCSELs. This is just because of the device self-heating as well as the presence of several unknown effects, e.g. QW Auger recombination in the device above threshold. Such heat-generating unknown effects introduces the non-linearity in the device PI characteristics measured at constant T_{hs}. By removing only the self-heating effect from other effects, it is possible to obtain the PI characteristics with a reduced non-linearity. For devices under study, we follow the wavelength method from [26] to obtain the *PI* characteristics at constant internal temperature. Figure 6 a) illustrates the contour curves of the device lasing wavelengths at different driving currents and heatsink temperature. Each constant emission wavelength curve indicates a constant internal temperature of the device which can be extracted by extrapolating those curves to $I = 0$. From Fig. 6 a), the internal temperature at which the laser turns off can be determined to be approximately 77°C which is the highest temperature the laser would work in pulsed mode. In order to verify this, the laser internal rollover temperature and turn off temperature defined by Eq. (8) and Eq. (9), respectively are plotted against the heatsink temperature as shown in Fig. 6 b).

$$T_{ro} = T_{hs} + P_{ro} R_{th} \tag{8}$$

$$T_{off} = T_{hs} + P_{off} R_{th} \tag{9}$$

The turn off temperature, T_{off} has been found to be 78°C, showing a good agreement with the value determined by the method mentioned earlier. As expected, the laser turn off tempera-ture, T_{off} is independent of heatsink temperature while the thermal rollover temperature, T_{ro} increases linearly with heatsink temperature. This is not surprising since the thermal rollover
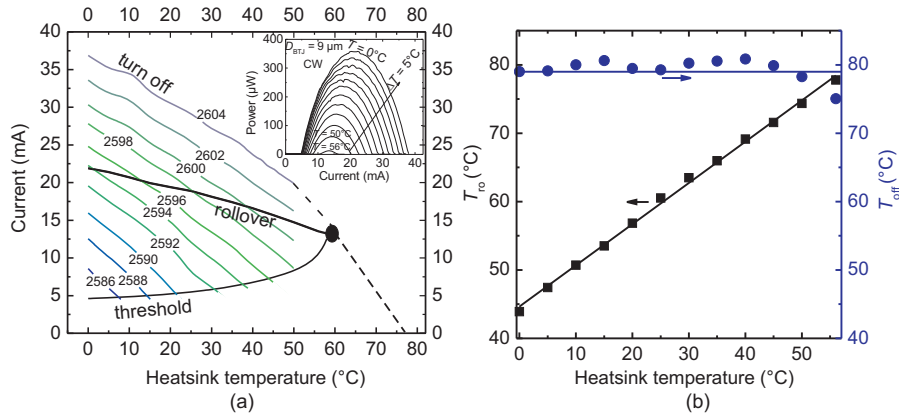
Fig. 6. a) Curves of constant laser emission wavelength at different driving current and heatsink temperature. Each constant wavelength curve represents the constant internal temperature of the device which can be extracted by extrapolating them to $I = 0$. The laser turn-off temperature can be determined to $\approx 77\,^{\circ}C$ which is independent of T_{hs}. Temperature dependent PI characteristics of the device with $D_{BTJ} = 9\,\mu m$ is shown in inset. The maximum CW operating heatsink temperature of the device is approximately 59°C. b) Internal rollover temperature (T_{ro}) and laser turn off temperatures (T_{off}) as a function a T_{hs}.

point is determined by not only the heatsink temperature and the amount of self heating caused by the applied electrical power but also with the applied driving current. Evidently, the device operated at lower heatsink temperature will be driven by more current to reach the thermal rollover than it would be for higher heatsink temperature. Then the slope (equivalent to the dif-
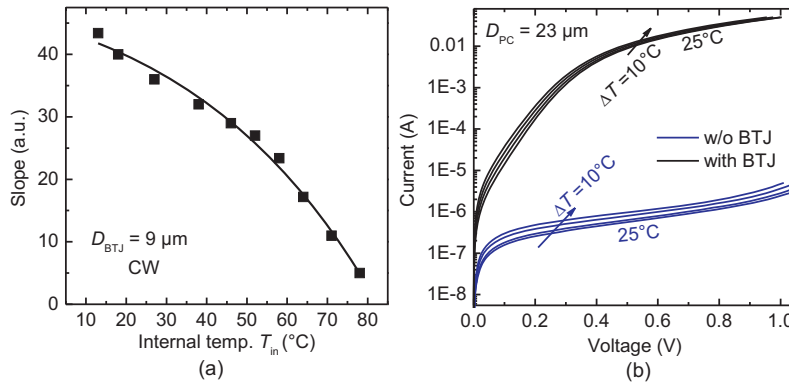

Fig. 7. a) The slope of the PI characteristics calculated at constant internal temperature as a function of internal temperature, T_{in}, b) Temperature dependent IV characteristics of the test structures with $D_{pc} = 23\,\mu m$ representing device central part with BTJ and outer part without BTJ in order to show the current confinement efficiency in VCSELs as a function of temperature.

ferential quantum efficiency) of the PI characteristics measured indirectly at constant internal temperature is plotted as a function of device internal temperature, T_{in}. As shown in Fig. 7 a) where we can see that the slope decreases with increasing T_{in}. This is not surprising either since several unknown effects, for instance, QW leakage current, QW Auger recombination and leakage current through the region outside of BTJ can take place in the QW region with increasing

temperature which has not been taken into account so far. The latter can be excluded from this discussion since the current confinement efficiency does not degrade in our devices with increasing temperature as demonstrated in Fig. 7 b). Here we measured the *IV* characteristics of a point contact test structure with diameter, $D_{pc} = 23\,\mu m$ in the region with BTJ and without BTJ. It was found that the ratio of the current in the region of BTJ to the region outside BTJ at a particular voltage of 0.8 is approximately 25,000 and this value remains almost constant with increasing temperature.

3.5. Internal quantum efficiency and losses

The laser parameters like internal quantum efficiency and internal losses have a significant effect on the device performance. Having an accurate knowledge on these parameters are extremely important for a realistic modeling of VCSELs. These two internal laser parameters are experimentally determined by the method mentioned in [27]. In our VCSELs, the mirror reflectivity of the dielectric outcoupling DBR is decreased by depositing additional *a*-Si layer on top. This results in an increased threshold current and differential quantum efficiency with higher mirror losses, as expected. The differential quantum efficiency η_d, the internal loss α_i and the internal quantum efficiency η_i are related to each other with the following equation:

$$\frac{1}{\eta_d} = \frac{\alpha_i}{\eta_i} \cdot \frac{1}{\alpha_m} + \frac{1}{\eta_i} \tag{10}$$

where α_m is the total mirror loss

$$\alpha_m = \frac{1}{2L_{eff}} \ln\left(\frac{1}{R_{oc}R_b}\right) \tag{11}$$

where L_{eff} is the effective cavity length, R_b and R_{oc} are the power reflectivities of the bottom and top mirror, respectively.

With only 4 pair SiO$_2$/*a*-Si dielectric DBR and by depositing additional 80 nm, 104 nm, 128 nm and 141 nm *a*-Si on top of that mirror which corresponds to a power reflectivity of 99.8%, 99.7%, 99.6%, 99.5% and 99.2%, respectively, the differential quantum efficiencies are measured from the *LI*-characteristics of single-mode VCSELs emitting at 2.6 μm at a heatsink temperature of 10° C and 0° C. Plotting $1/\eta_d$ against the calculated $1/\alpha_m$ and using a linear fit according to Eq. (10), $\eta_i = 40\%$ and $\alpha_i = 23.2\text{–}26\,\text{cm}^{-1}$ are obtained as illustrated in Fig. 8 a).

The reduced internal quantum efficiency in such laser could be attributed to several issues, such as hole confinement of the QWs, hole leakage by thermionic emission or inhomogeneous filling of the QWs by the carriers. The latter is rather unlikely since the conduction and valence band offsets are as low as $\Delta E_c^{QW} \approx 212\,\text{meV}$ and $\Delta E_{hh}^{QW} \approx 48\,\text{meV}$, respectively as shown in Fig. 8 b). Electrons remain very well confined in such QWs due to its moderately large conduction band offset, whereas E_{hh}^{QW} value is just less than twice of the thermal energy at room temperature (k_BT). Therefore, hole leakage by thermionic emission could be the most probable reason of the low η_i. Even the separate confinement layer Al$_{0.15}$GaAsSb does not help so much in confining the carriers into the active region since the valence band offset at the separate confinement layer E_{hh}^{SCH} is approximately twice as low as K_BT. The low η_i could also be due to the presence of well-known strong non-radiative Auger recombination effect at the long wavelength MIR lasers.

The extracted loss parameter, α_i contains all types of losses in the laser resonator. It includes out-coupling mirror losses, free carrier absorption in the cavity, the active region and epitaxial bottom Bragg mirror and diffraction loss. It should be noted that the deviation in α_i value as indicated in Fig. 8 a) is resulting from the measurement carried out at two different temperatures and partly due to the different current injection magnitude. This clearly indicates the presence
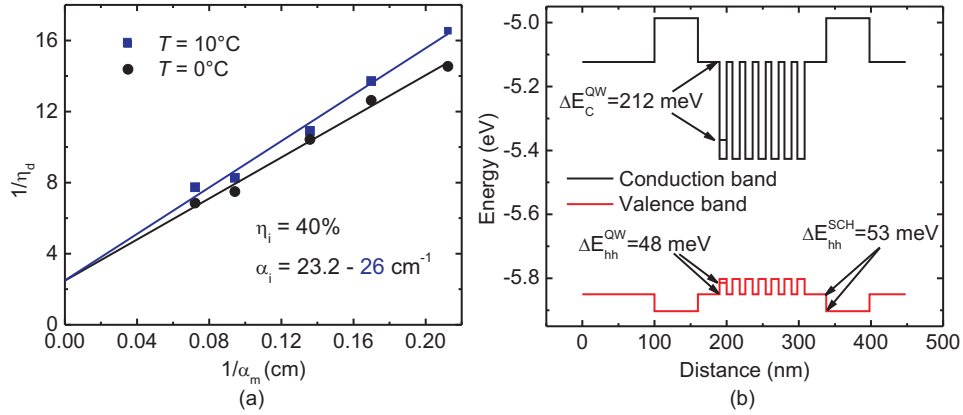
Fig. 8. a) Inverse differential quantum efficiency ($\eta_{\rm d}^{-1}$) against the inverse of mirror loss $\alpha_{\rm m}^{-1}$ in order to extract the internal parameters, $\eta_{\rm i}$ and $\alpha_{\rm i}$, Using a linear fit. b) Band diagram of the active region, consisting of quaternary InGaAsSb embedded in GaSb barriers, used in 2.6 μm VCSELs.

of temperature dependent loss mechanisms, e.g. Auger recombination, in the resonator. As expected, at 10°C the value of $\alpha_{\rm i}$ is higher than at 0°C since $\alpha_{\rm i}$ and $\eta_{\rm i}$ are both function of temperature.

3.6. Gain constant and transparency current

Gain constant ($g_{\rm o}$) for the active region material and transparency current density, $J_{\rm tr}$ are other two important laser parameters which can be determined experimentally. The gain and current density can be related by a semi-logarithmic function

$$g_{\rm th} = g_{\rm o} ln\left(\frac{\eta_{\rm i}J_{\rm th}}{N_{\rm QW}J_{\rm tr}}\right) \tag{12}$$

where $N_{\rm QW}$ is the number of QWs and $g_{\rm th}$ is the threshold gain.

In this work, both $J_{\rm th}$ and $g_{\rm th}$ of the device was changed by changing the outcoupling mirror reflectivity, while $g_{\rm th}$ is related to the reflectivity of outcoupling mirror by

$$g_{\rm th} = \frac{1}{\Gamma_{\rm z}}\left(\alpha_i + \frac{1}{2L_{\rm eff}}\ln\left(\frac{1}{R_{\rm oc}R_b}\right)\right) \tag{13}$$

where $\Gamma_{\rm z}$ is the longitudinal confinement factor which is calculated to be 0.037. Thus the calculated threshold gain are plotted as a function of measured threshold current density at a heatsink temperature of 0° C and 10° C as shown in Fig. 9 a). Logarithmic fitting using Eq. (13) yield values for g_0 and $J_{\rm tr}$.

In fact, $J_{\rm tr}$ sensitively depends on the sample quality and fabrication process and g_0 value obtained here is in a range and the measurement also involves some experimental inaccuracies. So, we recalculated these two laser parameters by an alternative experimental method.

This time $\eta_{\rm d}$ and $J_{\rm th}$ are measured for a number of devices with $5\,\mu{\rm m} \leq D_{\rm BTJ} \leq 16\,\mu{\rm m}$ at a constant internal temperature. And QW gain is related to $\eta_{\rm d}$ via

$$2N_{\rm QW}L_{\rm QW}\Gamma_{\rm r}g_{\rm th} = \frac{\eta_i T_{\rm oc}}{\eta_{\rm d}} \tag{14}$$
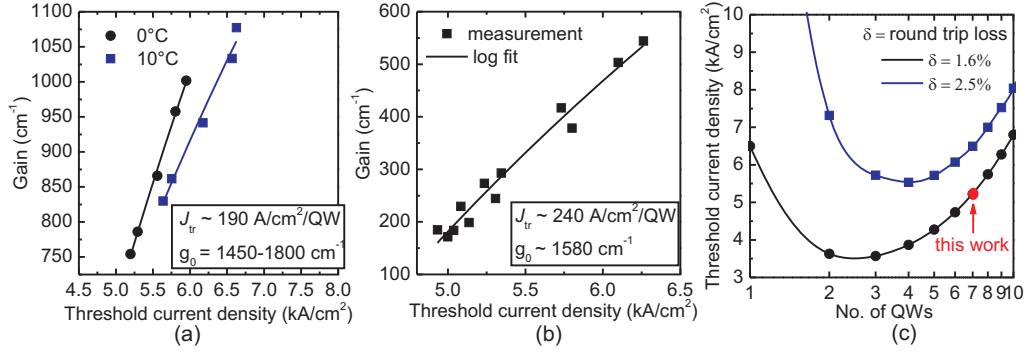
Fig. 9. a) Quantum well threshold gain against threshold current density for 2.6 μm VC-SELs with $D_{BTJ} = 8\,\mu m$ at 0° C and 10° C. The measured points are fitted using Eq. (12). b) Gain-current density curve for 2.6 μm VCSELs based on threshold gain variation with aperture diameter of the device. c) Calculated CW threshold current density as a function of number of QWs in the device.

where Γ_r is relative confinement factor, L_{QW} is the thickness of single QW, and T_{OC} is the transmission through the output mirror. The left and right side of Eq. (14) refers to total round trip gain in the active region and the round trip loss, δ of the device, respectively.

Thus we obtain a pair of numbers (g_{th}, J_{th}) where g_{th} is calculated using Eq. (14). As expected, both the threshold current and threshold current density will vary with the change of devices with different aperture diameters. As shown in Fig. 9 b), $g_o = 1580$ cm^{-1} and $J_{tr} = 240$ A/cm^2 per QW can be extracted by plotting these measured data and then fitting with logarithmic gain-current relation. Compared to GaAs-based material system, the higher gain coefficient value indicates that this material system exhibits excellent gain properties of the active region material [28].

With the known $g - J$ relationship we are in position to determine the optimum number of QWs for devices under study. Note that the round trip loss, δ is given by

$$\delta = 2N_{QW}L_{QW}\Gamma_r(N_{QW})g_{th}(J_{th}N_{QW}) \tag{15}$$

$$J_{th} = \frac{N_{QW}J_{tr}}{\eta_i}\exp\left(\frac{\delta}{2N_{QW}L_{QW}\Gamma_r g_0}\right) \tag{16}$$

For two different round trip cavity losses, the calculated CW threshold current density is plotted as a function of number of QWs as indicated in Fig. 9 c). An exemplary numerical calculation of the threshold current density, J_{th} for the device with $D_{BTJ} = 5\,\mu m$ is mentioned here which has been marked by a red dot in Fig. 9 c). Using Eq. (15) and $N_{QW} = 7$, $L_{QW} = 10$ nm, $\Gamma_r = 1.8$ and $g_{th} = 638$ cm^{-1}, one obtains the round trip loss, $\delta = 1.6\%$. The value of g_{th} can be calculated by Eq. (12) using $J_{th} = 5.2$ kA/cm^2, $\eta_i = 0.4$, $J_{tr} = 0.19$ kA/cm^2 and $g_o = 1450$ cm^{-1}. The round trip loss value δ can also be calculated by the right side of Eq. (14) and using measured $\eta_d = 7\%$, $\eta_i = 0.4$ and calculated $T_{OC} = 0.0024$. Finally one calculates CW threshold current density $J_{th} \approx 5.2$ kA/cm^2 using Eq. (16) and in good agreement with the measured value.

As can be seen in Fig. 9 c), with 1.6% round trip loss, the optimum number of well is 3, whereas 7 QW was used in presented devices. Therefore, reducing the number of QWs from 7 to 3, J_{th} will decrease and thus the device performance will be improved.

3.7. Measurement of water vapor concentration

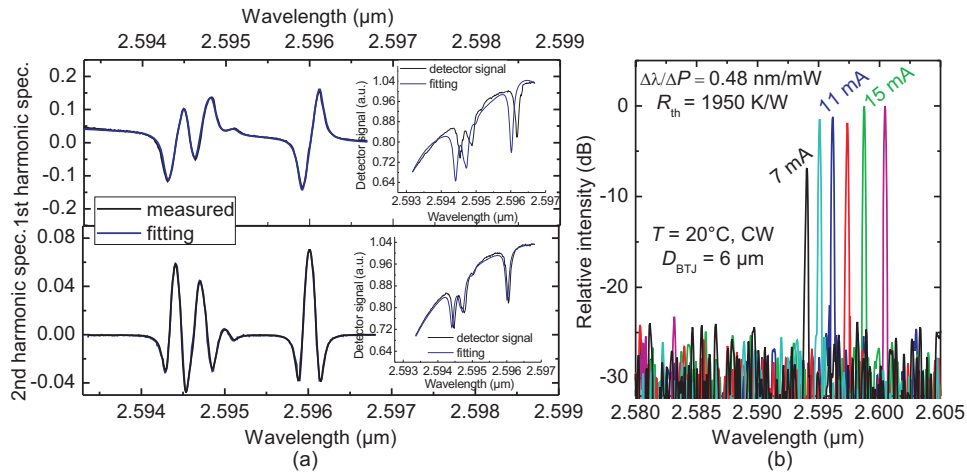Fig. 10. a) Measured WMS first and second harmonic spectra of H_2O absorption lines (black lines) and the fit using absorption line parameters from HITRAN database [1] (blue lines). The detected signal at the photodetector for VCSELs emitting at 2.6 μm and the fit extracted from corresponding first and second harmonic spectra as shown in inset. Due to the lack of the temperature stability in the measurement setup, a mismatch appears between these two signals. b) The driving current dependent emission spectra at $T = 20^\circ$C, showing the single-mode emission and the range of tunability.

An emission wavelength of 2.6 μm is of significant interest for gas detection by TDLAS. In fact, emission wavelengths of the presented lasers are obtained at 2.605, 2.596 and 2.594 μm where the strongest water vapor absorption lines are located. Such application-suited VCSELs open the way for gas measurements and isotopic ratio studies [29] by realizing absorption spectrometers with significant sensitivity improvements.

To prove the applicability of the VCSEL, an experiment was carried out in which the emission wavelength or intensity of the laser was modulated across the atmospheric water absorption features. This will show the suitability of such lasers in terms of modulation speed and stability of single-mode emission. The modulation was done by changing the driving current with an additional sinusoidal signal of frequency 10 kHz. This wavelength modulation spectroscopy method [30, 31] typically has a higher sensitivity for detecting the trace gases than direct absorption spectroscopy. In addition to its sensitivity, WMS has several other benefits which make it desirable over direct absorption spectroscopy due to the low spectral background.

In order to measure the atmospheric water vapor concentration, the first and the second harmonic (2f) spectra were recorded with the help of a lock-in amplifier which receives the intensity-modulated signal from the detector. Using the model in [31], the measured spectra are then fitted analytically as illustrated in Fig. 10 a). An absolute water vapor concentration of 1.5% in laboratory air was determined. The excellent fit proves that the laser exhibits single-mode operation and without mode-hops over the entire operating range (shown in Fig. 10 b) which is required for high resolution TDLS.

4. Conclusion

In conclusion, the issues related to design, characterization and applications of very long wavelength GaSb based BTJ VCSELs have been reported in this paper. Much emphasis has been laid

on the device characterization based on the theoretical and experimental investigations which allows to improve both the device design and performance. Despite of the fact that the GaSb-based material system (AlGaIn)(AsSb) is the material of choice for achieving highly reliable devices in the mid-infrared wavelength regime, the research on EP GaSb-based VCSELs is still at a preliminary stage. This work is directed toward addressing aspects of VCSEL design and performance that may be an input to the ongoing research and development efforts.